



Article

Miniature Ultrasound Transducer Incorporating Sm-PMN-PT 1-3 Composite

Jia-Ming Zhang ¹, Guo-Cui Bao ², Wen Gao ³, Ri-Qiang Lin ², Fan Yang ²  and Kwok-Ho Lam ^{2,4,*} 

¹ Department of Applied Physics, The Hong Kong Polytechnic University, Hong Kong, China; jiaming-george.zhang@connect.polyu.hk

² Department of Electrical and Electronic Engineering, The Hong Kong Polytechnic University, Hong Kong, China; guocbao@polyu.edu.hk (G.-C.B.); riqiang33.lin@connect.polyu.hk (R.-Q.L.); 18089114g@connect.polyu.hk (F.Y.)

³ College of Physics, University-Industry Joint Center for Ocean Observation and Broadband Communication, National Demonstration Center for Experimental Applied Physics Education, Qingdao University, Qingdao 266071, China; gaowen0317@163.com

⁴ Centre for Medical and Industrial Ultrasonics, James Watt School of Engineering, University of Glasgow, Glasgow G12 8QQ, UK

* Correspondence: kwokho.lam@glasgow.ac.uk

Abstract: Piezoelectric 1-3 composite materials have become extensively utilized in diagnostic ultrasound transducers owing to their high electromechanical coupling coefficient, low acoustic impedance, and low dielectric loss. In this study, Sm-doped PMN-PT ceramic/epoxy 1-3 composite with a ceramic volume fraction of 60% is fabricated by the dice-and-fill method, resulting in a high piezoelectric constant (650 pC/N) and clamped dielectric constant (2350). Utilizing the exceptionally high clamped dielectric constant, a low-frequency (12.4 MHz) ultrasound transducer is developed with a miniature aperture size (0.84 mm × 0.84 mm), exhibiting a −6 dB bandwidth of 70% and an insertion loss of −20.5 dB. The imaging capability of the miniature composite transducer is validated through both phantom and ex vivo imaging. The satisfactory results indicate that Sm-doped ceramic/epoxy composites possess significant potential for miniature devices in biomedical imaging applications.

Keywords: Sm-PMN-PT ceramics; ultrasound transducer; 1-3 composite; biomedical imaging



Citation: Zhang, J.-M.; Bao, G.-C.; Gao, W.; Lin, R.-Q.; Yang, F.; Lam, K.-H. Miniature Ultrasound Transducer Incorporating Sm-PMN-PT 1-3 Composite. *J. Compos. Sci.* **2024**, *8*, 80. <https://doi.org/10.3390/jcs8030080>

Academic Editor: Francesco Tornabene

Received: 15 January 2024

Revised: 4 February 2024

Accepted: 19 February 2024

Published: 22 February 2024



Copyright: © 2024 by the authors. Licensee MDPI, Basel, Switzerland. This article is an open access article distributed under the terms and conditions of the Creative Commons Attribution (CC BY) license (<https://creativecommons.org/licenses/by/4.0/>).

1. Introduction

Ultrasound imaging holds a crucial role in the biomedical field, owing to its non-invasive and radiation-free characteristics [1,2]. The ultrasound transducer stands out as a critical factor in determining imaging quality, as it facilitates the conversion of electrical energy into mechanical energy and vice versa [3]. Piezoelectric ceramic materials, notably lead zirconate titanate (PZT), exhibit remarkable piezoelectric properties and stability [4,5], making them a popular choice as the active layer in ultrasound transducers. However, one limitation of ceramic materials is their relatively high acoustic impedance (>30 MRayl), in contrast to the low acoustic impedance of biological tissues (~1.5 MRayl). This acoustic impedance mismatch can result in ultrasound transducer performance degradation. To address this issue, carefully designed matching layers with specific thicknesses become essential. These layers aim to enhance the acoustic transmission rate between the transducer's front surface and biological tissues, ensuring optimal ultrasound imaging performance [6].

To overcome the aforementioned challenge, piezoelectric composite materials have been employed, aiming for lower acoustic impedance, higher electromechanical coupling coefficients, and reduced dielectric losses [7]. These composites involve the integration of both piezoelectric and polymer materials, forming either 1-3 or 2-2 connectivity configurations [8]. The 1-3 composite, known for its superior effective thickness coupling

performance, has found widespread use in ultrasound transducer development [9,10]. Initially, PZT/epoxy-based 1-3 composites were extensively investigated and are now still widely used for biomedical ultrasound imaging applications [11,12]. In addition to conventional PZT ceramics, extensive research has been conducted on lead-free piezoelectric ceramics for the application of ultrasound transducers, particularly in the form of 1-3 composites. Barium-modified bismuth sodium titanate, $0.94(\text{Bi}_{0.5}\text{Na}_{0.5})\text{TiO}_3\text{-}0.06\text{BaTiO}_3$ (BNT) fibers were derived using the sol-gel method to develop a 15-MHz 1-3 composite ultrasound transducer [13]. Chen et al. explored the use of manganese-doped $0.7\text{BiFeO}_3\text{-}0.3\text{BaTiO}_3$ ceramics for ultrasound transducer development, demonstrating its potential for practical applications [14]. Potassium sodium niobate (KNN)-based ceramics, known for their high piezoelectric performance among lead-free ceramics, were also investigated. With Fe_2O_3 -modified KNN ceramics, a broadband ultrasound transducer based on the corresponding composite was successfully developed [15]. While these composites demonstrated an improved electromechanical coupling coefficient compared to bulk ceramic materials, the piezoelectric constant was compromised due to the passive nature of epoxy, which did not contribute to vibration during the piezoelectric effect. Consequently, the sensitivity of 1-3 composite-based ultrasound transducers, particularly unfocused ones, was deemed unsatisfactory [16].

To enhance the performance of 1-3 composites, there arose a demand for piezoelectric ceramics with high piezoelectric constants. In recent years, rare-earth-doped $(1-x)\text{Pb}(\text{Mg}_{1/3}\text{Nb}_{2/3})\text{O}_3\text{-}x\text{PbTiO}_3$ (PMN-PT) has emerged as a promising candidate, demonstrating substantial improvements in piezoelectric constants. For instance, ceramics doped with europium (Eu) or samarium (Sm) can achieve piezoelectric constants exceeding 1000 pC/N [17,18]. These materials also exhibit high dielectric constants, a desirable feature for miniature biomedical ultrasound transducers.

In this study, 2.5%Sm-0.72PMN-0.28PT with high piezoelectric coefficient and dielectric permittivity was synthesized. A high-frequency 1-3 composite was then fabricated using the dice-and-fill method for the development of a miniature ultrasound transducer. With the high dielectric permittivity, the aperture size of the transducer was significantly reduced but retained a satisfying bandwidth and sensitivity. Spatial resolution was measured to verify the transducer performance. The *ex vivo* imaging was also conducted to show potential for biomedical imaging applications.

2. Materials and Methods

2.1. Preparation and Characterizations

With Pb_3O_4 , Sm_2O_3 , $\text{Mg}_2(\text{OH})_2\text{CO}_3$, Nb_2O_5 , and TiO_2 as raw materials, 2.5%Sm-0.72PMN-0.28PT was synthesized along with our previous optimized method [19]. Two kinds of pre-calcination powders, one with a rhombohedral phase and the other with a tetragonal phase were initially prepared at $880\text{ }^\circ\text{C}$ for 4 h. Subsequently, they were mixed and sintered at $1250\text{ }^\circ\text{C}$ for 1.5 h, following the designated proportions to synthesize the target composition of $\text{Pb}_{0.9625}\text{Sm}_{0.025}(\text{Mg}_{1/3}\text{Nb}_{2/3})_{0.72}\text{Ti}_{0.28}\text{O}_3$. To test the piezoelectric and dielectric properties of the ceramics, silver paste was applied to both surfaces and sintered at $650\text{ }^\circ\text{C}$ for 30 min to form electrodes. After being poled at 3 kV/mm for 10 min and undergoing an aging treatment for 24 h, the electrical properties were measured.

The crystal structures and morphologies of the samples were characterized using X-ray powder diffraction (XRD, Rigaku, Tokyo, Japan) and scanning electron microscopy (SEM, JSM-6510, JEOL, Tokyo, Japan), respectively. After co-fired silver electrodes on both surfaces of ceramic disk, the ferroelectric hysteresis loop was measured at room temperature. The piezoelectric coefficient (d_{33}) was measured using a quasi-static d_{33} tester (ZJ-6A, Chinese Academy of Science, Beijing, China). The dielectric properties and electromechanical coupling coefficient (k_t) were measured by an impedance analyzer (HP4294A, Agilent, Santa Clara, CA, USA).

To determine the acoustic impedance of ceramics, the measurements of longitudinal sound velocity (c) and density (ρ) were conducted. The density of samples was determined

using the Archimedes drainage method. For the longitudinal sound velocity, two commercial 5-MHz ultrasound transducers were positioned at opposite sides with a specific distance and immersed in distilled water. One transducer was excited by a pulser/receiver to transmit signals, while the other received the signals. The time-of-flight results of ultrasound signals were recorded both with and without inserting the ceramic sample between the two transducers. The longitudinal sound velocity (c_{sample}) was then calculated as:

$$\tau_{\text{water}} - \tau_{\text{sample}} = t \left(\frac{1}{c_{\text{water}}} - \frac{1}{c_{\text{sample}}} \right),$$

where c_{water} and c_{sample} are sound velocities in water and sample, respectively, τ_{water} and τ_{sample} are the times for receiving signals without and with the sample, respectively, and t is the thickness of the sample.

2.2. Design and Fabrication of 1-3 Composites

To achieve high-frequency 1-3 composites, the diced kerfs should be sufficiently thin. In this study, a ZH05-AA (DISCO Co., Ltd., Omori-Kita, Tokyo, Japan) blade was employed to achieve a kerf width of 21 μm . After determining the kerf width, the ceramic pillar width can be calculated through the below equation of ceramic volume fraction (ϕ):

$$\phi = \frac{(\text{ceramic pillar width})^2}{(\text{ceramic pillar width} + \text{kerf width})^2}.$$

The volume fraction was determined as ~60% to retain good piezoelectric performance such that the ceramic pillar width was set as 72 μm . To mitigate the lateral vibration modes, the final thickness of 1-3 composites was lapped down to 96 μm , ensuring the attainment of a specific width-to-height aspect ratio.

A conventional dice-and-fill method, as depicted in Figure 1, was commonly employed to fabricate the 1-3 composites [20,21]. The unpoled bulk piezoelectric ceramic (1 mm thick) was initially diced with a pitch of 93 μm in one direction, with a dicing depth of ~300 μm . Subsequently, low-viscosity epoxy (EPO-TEK 301, Epoxy Tech., Billerica, MA, USA) was applied to fill the diced kerfs. After curing for 24 h at room temperature, excess epoxy was removed through lapping and polishing. The same dicing procedure was then repeated in the direction perpendicular to the initial dicing, followed by the same filling method. Finally, the entire stack was lapped from the other side of the ceramic to remove the bulk ceramic part. Poling was conducted after dicing and lapping, as these processes may lead to the depolarization of ceramic with a relatively low Curie temperature [22].

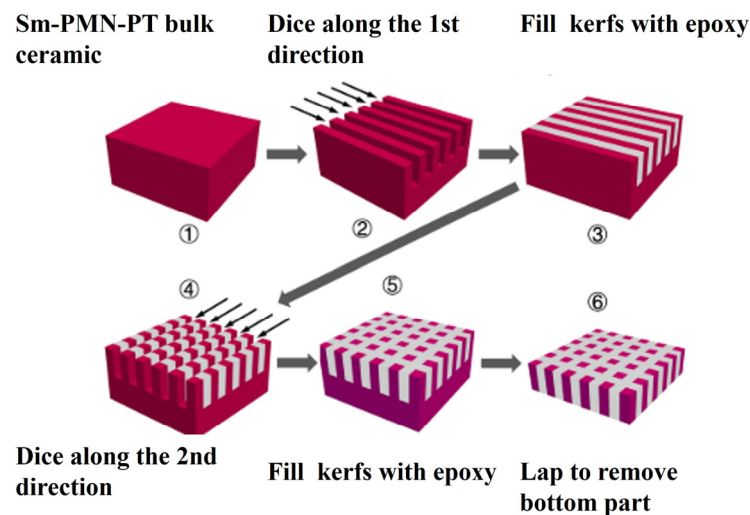


Figure 1. Dice-and-fill method for the fabrication of 1-3 composite [16].

The characteristics of composite material were measured, including d_{33} , k_t , and clamped dielectric constant (ϵ^s). Based on electrical impedance/phase spectra, k_t can be calculated as:

$$k_t = \sqrt{\frac{\pi f_r}{2 f_a} \tan\left(\frac{\pi f_a - f_r}{2 f_a}\right)},$$

where f_r and f_a are resonant frequency and anti-resonant frequency, respectively. In transducer design, achieving an electrical impedance of near 50 Ω for effective electrical matching, and this impedance is closely related to ϵ^s . The measurement of ϵ^s involves analyzing series capacitance and dissipation curves, as expressed:

$$\epsilon^s = \frac{C^s t}{A},$$

where C^s is the series capacitance at a frequency that is twice the resonant frequency, and t and A are the thickness and aperture size, respectively, of the composite material. To achieve effective electrical matching, the aperture size was calculated as:

$$A = \frac{t}{2\pi\epsilon^s\epsilon_0 f_r Z'},$$

where ϵ_0 is the permittivity at vacuum (8.854×10^{-12} F/m), and Z was set as 50 Ω .

2.3. Fabrication and Evaluation of Transducer

PiezoCAD software (3.06) was employed for transducer performance simulation. Based on the Krimholtz, Leedom, and Mattaei (KLM) model, PiezoCAD could provide an optimized design for ultrasound transducers. In this study, E-solder 3022 (Von Roll Isola Inc., Schenectady, NY, USA) silver epoxy was employed as the backing layer due to its electrical conductivity and high acoustic attenuation. A single matching layer has been commonly employed to enhance the performance of ultrasound transducer, whose ideal acoustic impedance could be expressed as:

$$Z_{\text{matching layer}} = Z_0^{1/3} Z_1^{2/3},$$

where Z_0 and Z_1 are acoustic impedances of piezoelectric composite and biological tissues (1.5 MRayl), respectively [23]. Vapor-deposited parylene was selected as the single matching layer not only for its proper acoustic impedance but also for its waterproof properties.

The transducer fabrication process follows the conventional ultrasound transducer technology: An unpolarized 2.5%Sm-0.72PMN-0.28PT was firstly diced and filled to form a 1-3 composite structure, which was then lapped to 96 μm . After polishing the surface, a Cr/Au electrode was sputtered onto it. E-solder was subsequently cast on the surface, using a centrifuge at 2000 rpm for 15 min to ensure connectivity throughout the whole aperture. After curing overnight, the backing layer was lapped down to ~ 0.5 mm. The other side of composite was also polished and electroded. The acoustic stacks were diced to the desired aperture size with a square shape. A co-axial cable was used for electrode connection on both sides of composite with E-solder. The stack connected to the cable was then placed into a stainless-steel tube, with epoxy for isolation and stabilization. The parylene layer was deposited with the desired thickness. Finally, an electric field was applied through the co-axial cable to pole the transducer in the air. A schematic cross-section diagram of the transducer is illustrated in Figure 2.

The pulse-echo response was measured to determine the center frequency (f_c) and bandwidth (BW) of the developed transducer. The transducer was immersed into distilled water and excited by a pulse/receiver (Panametrics 5900PR, Olympus, Tokyo, Japan) with 1 μJ energy, while the echo signal was acquired by a digital oscilloscope with 50 Ω damping (HP Infinium DSO-S204A, Keysight Technologies, Santa Rosa, CA, USA). The

fast Fourier transform (FFT) was employed to transfer the time-domain echo signals to a frequency-domain spectrum. f_c and BW can be determined as:

$$f_c = \frac{f_1 + f_2}{2},$$

$$BW = \frac{f_2 - f_1}{f_c} \times 100\%,$$

where f_1 and f_2 are lower and upper -6 dB frequencies, respectively. The effective electromechanical coupling coefficient (k_{eff}) was calculated as:

$$k_{\text{eff}} = \sqrt{1 - \frac{f_r^2}{f_a^2}}.$$

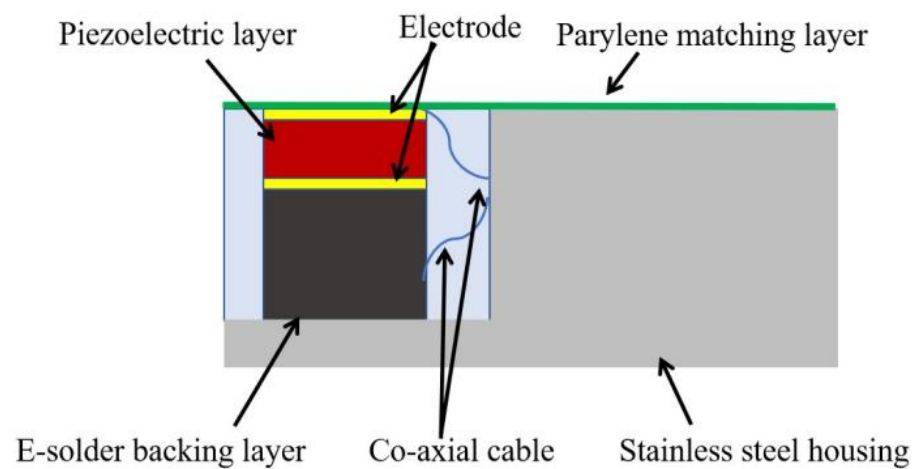


Figure 2. Cross-sectional illustration of transducer.

Two-way insertion loss (IL) was also measured by exciting a transducer through a function generator (AFG3251, Tektronix, Beaverton, AL, USA), where a burst of a 10-cycle sinusoidal wave with a frequency of f_c was generated with 50Ω coupling. The echo signal, reflected by a quartz plate, was recorded by a digital oscilloscope with $1 \text{ M}\Omega$ coupling. IL was then calculated as [24]:

$$IL = 20\log\left(\frac{V_1}{V_0}\right) + 1.9 \text{ dB} + 2.2 \times 10^{-4} \times f_c^2 \times 2d,$$

where V_0 and V_1 are peak-to-peak voltages of the emitted signal and received echo signal, respectively. A total of 1.9 dB represents the loss of ultrasound signal at the quartz surface, while $2.2 \times 10^{-4} \text{ (dB/cm}\cdot\text{MHz}^2)$ is the attenuation coefficient of ultrasound signal in water.

Imaging experiments were then conducted to evaluate the performance of 1-3 composite transducers, wherein lateral and axial resolutions were measured. Theoretically, the lateral resolution of ultrasound mainly depends on the dimensions of the transducer, while f_c and BW determine the axial resolution as follows:

$$R_{\text{lateral}} = \frac{\lambda F}{d},$$

$$R_{\text{axial}} = 0.5 \frac{c}{f_c \times BW},$$

where λ and c are the acoustic wavelength and acoustic velocity in water, respectively, d is the diameter of the acoustic stack, and F is the focal length. For an unfocused transducer, its focal length is the near-field distance (N) as:

$$N = \frac{d^2 f_c}{4c}$$

Four 10 μm -diameter tungsten wires were arranged at different heights in a 3D-printed holder. The wire phantom was immersed in distilled water for imaging acquired by the transducer. With a step motor (a step size of 5 μm) triggered by the pulse/receiver, the transducer was horizontally moved for scanning. A dynamic range of 26 dB was employed during imaging. Analyzing a cross-sectional ultrasound image of tungsten wire, the lateral and axial resolutions were assessed along specific directions using the full width at half maximum (FWHM).

The ex vivo sample was prepared with biological tissue and metal [25]. Raw chicken breast purchased from the local market was used as the tissue. A 1.6 mm-diameter metal needle was inserted into the chicken breast for evaluating the imaging capability of transducer.

3. Results and Discussion

3.1. Ceramic Properties

The XRD pattern and Rietveld refinement of 2.5%Sm-0.72PMN-0.28PT ceramics are shown in Figure 3. The XRD result of 2.5%Sm-0.72PMN-0.28PT ceramics shows a pure perovskite structure (PDF card No. 39-1487) without the involvement of a second phase. Both (110) and (002) peaks were single peaks with good symmetry, indicating the coexistence of rhombohedral and tetragonal phases [26]. This was attributed to the preparation process in which a mixture of two different crystalline phases was sintered to precisely control the phase proportion, thus forming a crystalline structure that resembles morphotropic phase boundaries (MPB). It is generally recognized that ceramics perform excellent electrical properties at the MPB [27]. The Rietveld refinement was performed to further investigate the crystalline structure of the ceramics. The results show that the 2.5%Sm-0.72PMN-0.28PT ceramics featured a mixture of the 40% tetragonal phase and the 60% rhombohedral phase, which was completely in agreement with the above analysis.

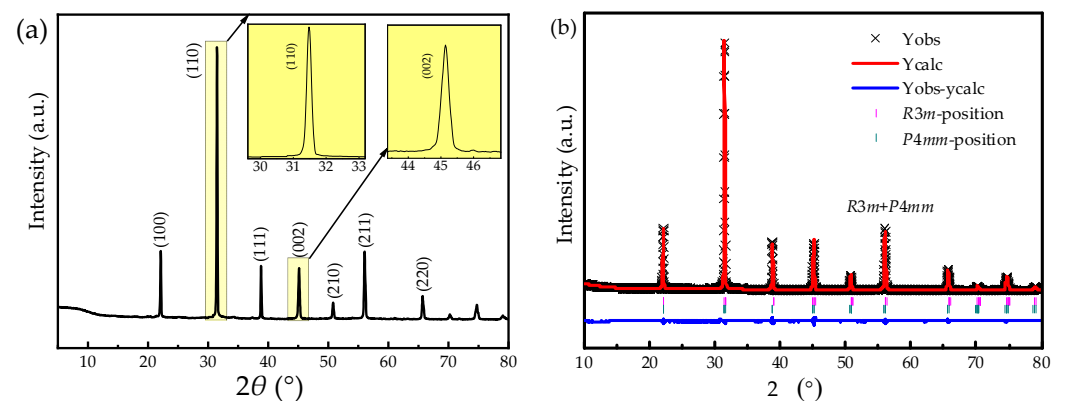


Figure 3. (a) XRD pattern and (b) Rietveld refinement of 2.5%Sm-0.72PMN-0.28PT ceramics.

The SEM micrograph of 2.5%Sm-0.72PMN-0.28PT ceramic is shown in Figure 4. The inset shows the distribution of grain size that obeys the Gaussian-shaped distribution and gives an average grain size of 4.95 μm . All cross-sectional morphology showed homogeneous and dense ceramic grains. Moreover, there were no visible pores and impurities in the morphology, indicating the well-developed ceramic grains.

The temperature-dependent dielectric spectra of 2.5%Sm-0.72PMN-0.28PT ceramics at different frequencies are shown in Figure 5. It is obvious that the phenomena of dispersive phase transition (broadened dielectric and loss peaks) and frequency dispersion (dielectric and loss peaks move towards higher temperatures with increasing frequency) are the characteristics of relaxor ferroelectrics [28]. The Curie temperature T_c of 2.5%Sm-0.72PMN-0.28PT ceramics was 81 $^{\circ}\text{C}$, representing the temperature at which the phase transition

occurs from a ferroelectric phase to a paraelectric phase at 1 kHz. The corresponding dielectric peak value reached 30,192 at 1 kHz.

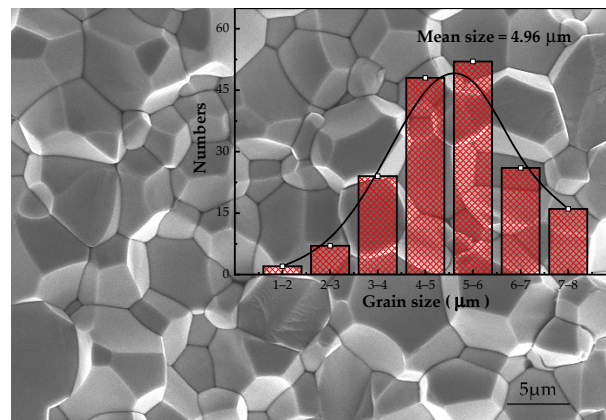


Figure 4. SEM micrograph and (inset) grain size statistics of 2.5%Sm-0.72PMN-0.28PT ceramics.

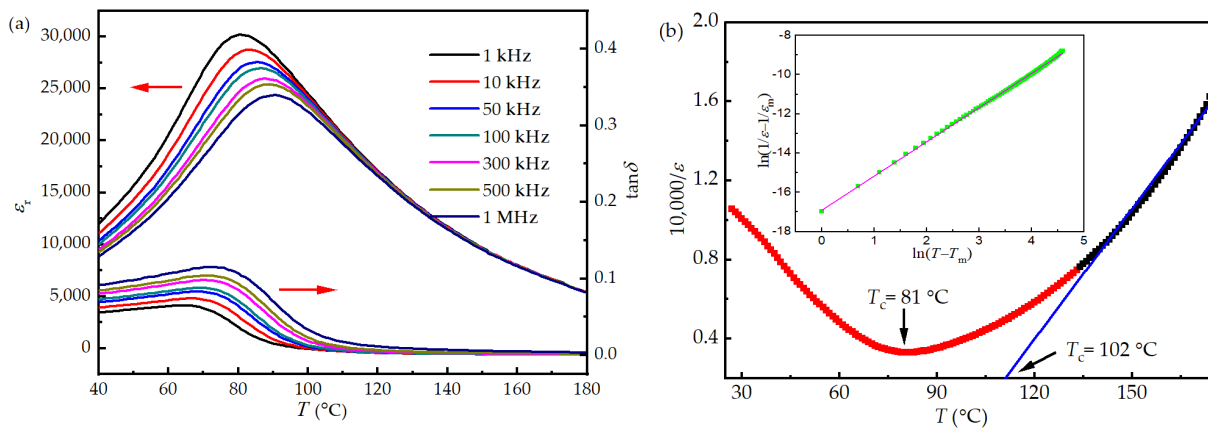


Figure 5. (a) Temperature-dependent dielectric spectra and (b) Curie–Weiss plot for the temperature-dependent dielectric spectra at 1 kHz (the inset shows the quadratic law fitting result for the temperature-dependent dielectric spectra at 1 kHz) of 2.5%Sm-0.72PMN-0.28PT ceramics.

The temperature dependence of the dielectric constant of ceramics can be characterized by the Curie–Weiss law [29]:

$$\epsilon = \frac{C}{T - T_0}$$

or quadratic law [30]:

$$\frac{1}{\epsilon} = \frac{1}{\epsilon_{\max}} + \frac{(T - T_c)^\gamma}{C'}$$

where C is the Curie–Weiss constant, T_0 is the Curie–Weiss temperature, γ is the relaxation index, and C' is a constant. The fitting results of the Curie–Weiss law and quadratic law for the temperature-dependent dielectric spectra at 1 kHz are shown in Figure 5b. According to the Curie–Weiss plot, the ferroelectric transition temperature (T_C) and Curie–Weiss temperature (T_0) were determined to be 102 °C and 81 °C, respectively. The deviations of T_C and T_0 manifest the typical characteristics of relaxor ferroelectric materials: broadened dielectric peaks rather than sharp ones. Regarding the quadratic law, when γ approaches 1, it indicates a normal ferroelectric, whereas an approach towards 2 indicates a relaxing ferroelectric. The fitting result yielded a relaxation index of 1.83, indicative of obvious relaxation characteristics.

The ferroelectric properties of 2.5%Sm-0.72PMN-0.28PT ceramics are shown in Figure 6. It can be seen that the P-E loop exhibits great symmetry with the remanent polarization

strength of $23.21 \mu\text{C}/\text{cm}^2$, showing good ferroelectric properties. Moreover, the coercive field was $0.27 \text{ kV}/\text{mm}$, indicating that the polarization process could be completed at a relatively low electric field [31]. The overall piezoelectric and dielectric properties of 2.5%Sm-0.72PMN-0.28PT ceramic at room temperature are listed in Table 1.

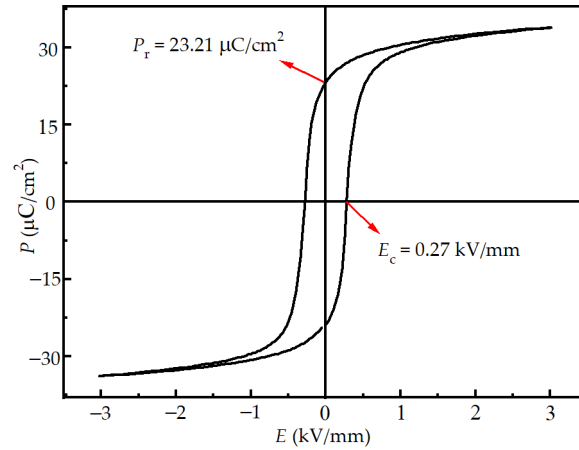


Figure 6. P-E hysteresis loop of 2.5%Sm-0.72PMN-0.28PT ceramics.

Table 1. Properties of 2.5%Sm-0.72PMN-0.28PT ceramics at room temperature.

d_{33} (pC/N)	k_t	ϵ_{33}/ϵ_0	ρ (kg/m ³)	c (m/s)	Z (MRayl)
1025	0.51	12,006	7.9	4100	32.4

3.2. Composite Properties

Figure 7 shows a photograph of a fabricated 1-3 composite taken with high-resolution optical microscopy. The kerf width was measured as $21 \mu\text{m}$, and the ceramic pillar was measured as $72 \mu\text{m}$. The ceramic volume fraction was calculated as 59.9%, which correlates well with the designed parameters.

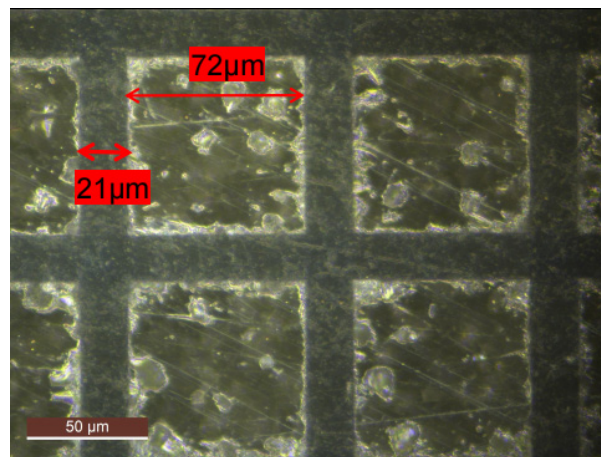


Figure 7. Optical image of Sm-PMN-PT 1-3 composite.

Piezoelectric and dielectric properties of 1-3 composites are summarized in Table 2. Compared to other reported ceramic/epoxy 1-3 composites, d_{33} and ϵ^s of composite in this study were significantly high due to the excellent properties of Sm-PMN-PT ceramics, while maintaining the coupling coefficient. Thus, the 1-3 composites demonstrate great potential for the development of miniature ultrasound transducers with high sensitivity.

Table 2. Properties comparison of reported 1-3 composite materials and this work.

Material	d_{33}	ϵ_{33}/ϵ_0	k_t	ϕ (%)
PZT-5H 1-3 composite [32]	390	557	0.68	60
Mn-doped BFO-BTO 1-3 composite [13]	45	/	0.46	60
NKLKT 1-3 composite [33]	140	/	/	25
Fe-KNN-based 1-3 composite [21]	340	513	0.59	62
KNNS-BNZH 1-3 composite [15]	350	/	0.70	61
Sm-PMN-PT 1-3 composite (This work)	650	2350	0.67	60

3.3. Simulation and Measurement of Transducer

Based on the high ϵ^s value, a miniature ultrasound transducer was designed with an aperture size of 0.84 mm × 0.84 mm. The design parameters of materials used for transducer development are listed in Table 3, while the simulated pulse–echo response and impedance spectra are shown in Figure 8. According to the simulation results, electrical matching could be achieved with a miniature aperture size of 1-3 composites. The simulated f_c and -6 dB BW were 14.3 MHz and 79%, respectively.

Table 3. Properties of 1-3 composite and passive materials.

Material	t (μm)	A (mm)	Z (MRayl)	Usage
Sm-PMN-PT Composite	96	0.84 × 0.84	19.4	Piezoelectric layer
E-solder 3022	500	0.84 × 0.84	5.6	Backing layer
Parylene	30	N/A	2.7	Matching layer

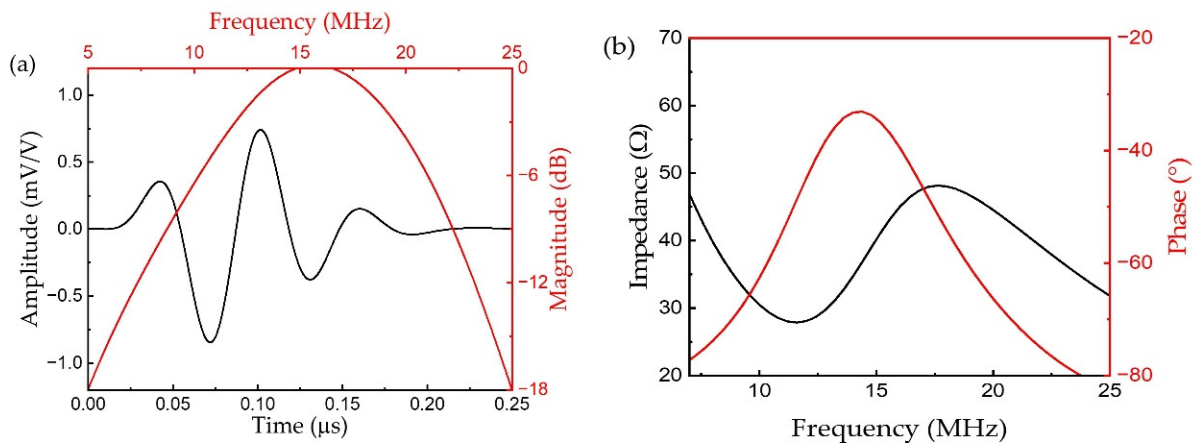


Figure 8. Simulated (a) pulse–echo response and (b) electrical spectra of transducer incorporating Sm-PMN-PT 1-3 composite.

The fabricated transducer prototype is shown in Figure 9. Figure 10a,b shows the measured pulse–echo response and impedance/phase spectra of the transducer, respectively. It was found that f_c was 12.4 MHz and BW was ~70%. Furthermore, the electrical impedance at f_c was close to the optimized value (~50 Ω). In addition, k_{eff} was calculated as 0.66.

Table 4 compares the performance of transducers fabricated using various 1-3 composites. Among the transducers with similar f_c , the aperture size presented in this work was significantly small but with the optimized electrical impedance, which is attributed to the high ϵ^s of Sm-PMN-PT ceramics. Compared with the reported work as listed in Table 4, k_{eff} and BW of transducer incorporating Sm-PMN-PT based 1-3 composite was relatively high.

The sensitivity of the transducer was also measured, showing an IL value of -20.5 dB. As listed in Table 5, the composite transducer developed in this work exhibited high sensitivity when compared to other reported transducers with similar configurations, which is attributed to the outstanding piezoelectric performance of Sm-PMN-PT ceramics.

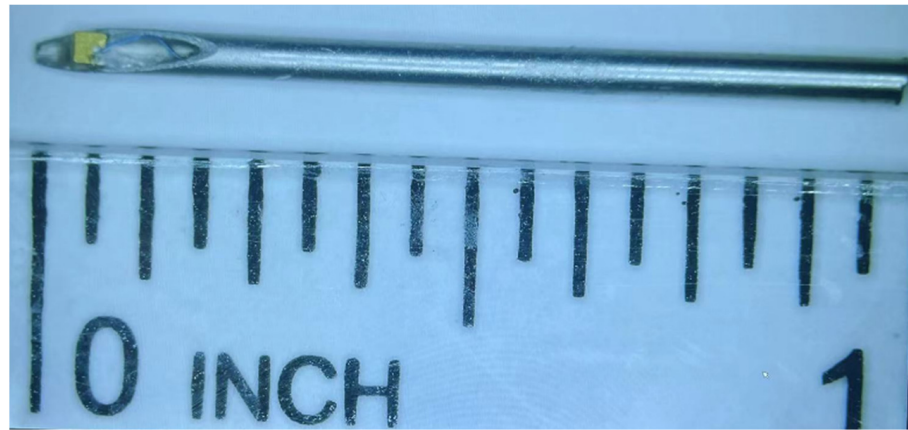


Figure 9. Photograph of fabricated miniature ultrasound transducer using Sm-PMN-PT 1-3 composite.

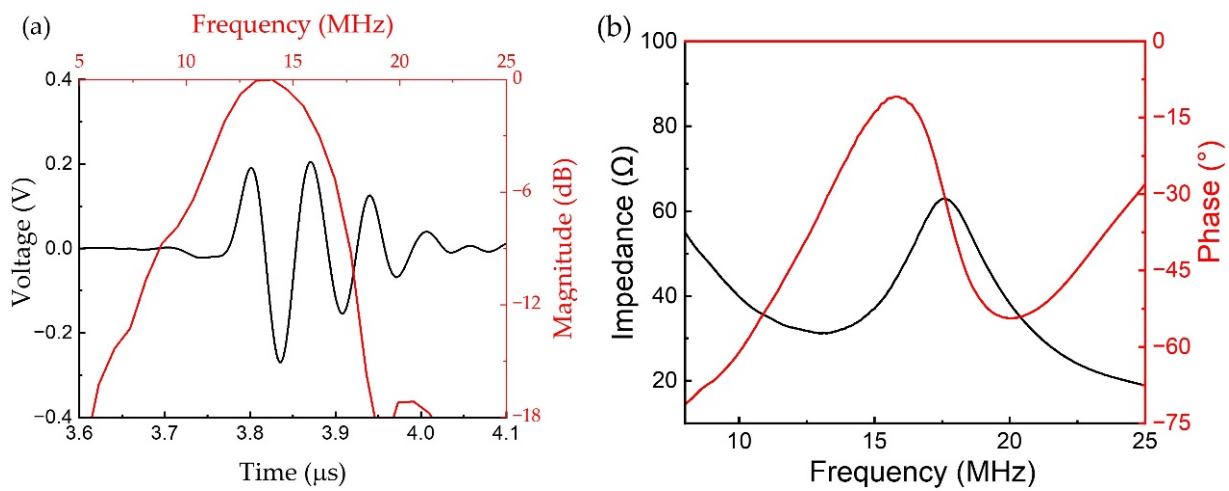


Figure 10. Measured (a) pulse–echo response and (b) electrical impedance spectra of transducer incorporating Sm-PMN-PT 1-3 composite.

Table 4. Performance comparison of ultrasound transducers fabricated using various 1-3 composites.

Transducer Material	f_c (MHz)	BW (%)	A (mm ²)	k_{eff}	Electrical Impedance (Ω)
PZT-5H 1-3 composite [32]	13.5	/	3.5 × 3.5	0.56	~50
PZT-5H 1-3 composite [34]	13.0	59	3.0 × 1.5	/	/
Fe-KNN 1-3 composite [21]	16.0	83	Ø 2.7	0.55	~50
KNN 1-3 composite [35]	23.0	75	Ø 2.5	0.50	~50
Sm-PMN-PT 1-3 composite (This work)	12.4	70	0.84 × 0.84	0.66	~50

Table 5. Comparisons of matching layer material and sensitivity of ultrasound transducers fabricated using various 1-3 composites.

Transducer Material	Matching Layer	IL (dB)
PZT 1-3 composite [36]	Silver epoxy	−34.0
BNT 1-3 composite [13]	N/A	−34.8
BTO 1-3 composite [13]	Al ₂ O ₃ /epoxy	−33.5
KNN 1-3 composite [33]	1st: Silver epoxy & 2nd: Polymer	−25.1
KNNS-BNZH 1-3 composite [15]	Epoxy	−30.0
Sm-PMN-PT 1-3 composite (This work)	Parylene	−20.5

It was observed that the sensitivity of the transducer was affected by the miniature aperture, limiting the emitted acoustic pressure. The miniature ultrasound transducer exhibited lower emitted acoustic pressure compared to a transducer with a similar f_c but a larger aperture size. Consequently, the received acoustic pressure of the echo signal was relatively weak, resulting in a high IL value. Additionally, miniature transducers, in general, tend to show a larger measured IL (magnitude) compared to simulation results based on the KLM model [37]. Despite these challenges, the sensitivity of the Sm-PMN-PT-based 1-3 composites transducer remained satisfactory, demonstrating comparable performance to miniature transducers fabricated using piezoelectric ceramics [38].

A scanned image of four 10 μm -diameter tungsten wires is shown in Figure 11a. The first tungsten wire was analyzed with the aforementioned method. Both the axial and lateral resolutions were 70 μm and 350 μm , respectively, which were analyzed from the first tungsten wire image with the corresponding FWHMs shown in Figure 11b,c. Both measured axial and lateral resolutions correlated well with theoretical values (85 μm ; 317 μm). The chicken breast inserted with a metal needle, as shown in Figure 12a, was employed as the biological sample of ex vivo imaging. The image (Figure 12b) clearly shows the tissue structure of the chicken breast and the location of the metal needle. The needle was clearly displayed with significantly different signal intensity compared with surrounding tissues, demonstrating the in vitro imaging capability of a miniature transducer. Moreover, the transducer was configured as the prototype of a side-looking catheter. The aforementioned results indicate promising potential for its application in endoscopy for the gastrointestinal tract [39].

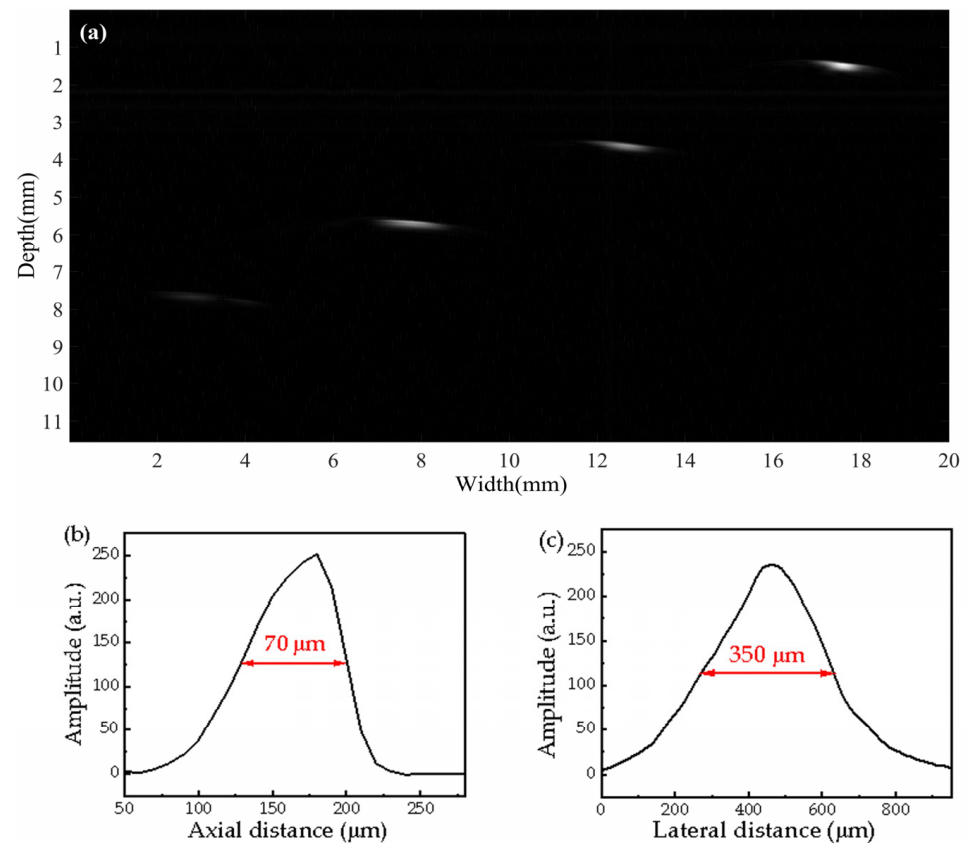


Figure 11. (a) Ultrasound image of tungsten wires with a dynamic range of 26 dB, and the measured (b) axial and (c) lateral resolutions of miniature transducer.

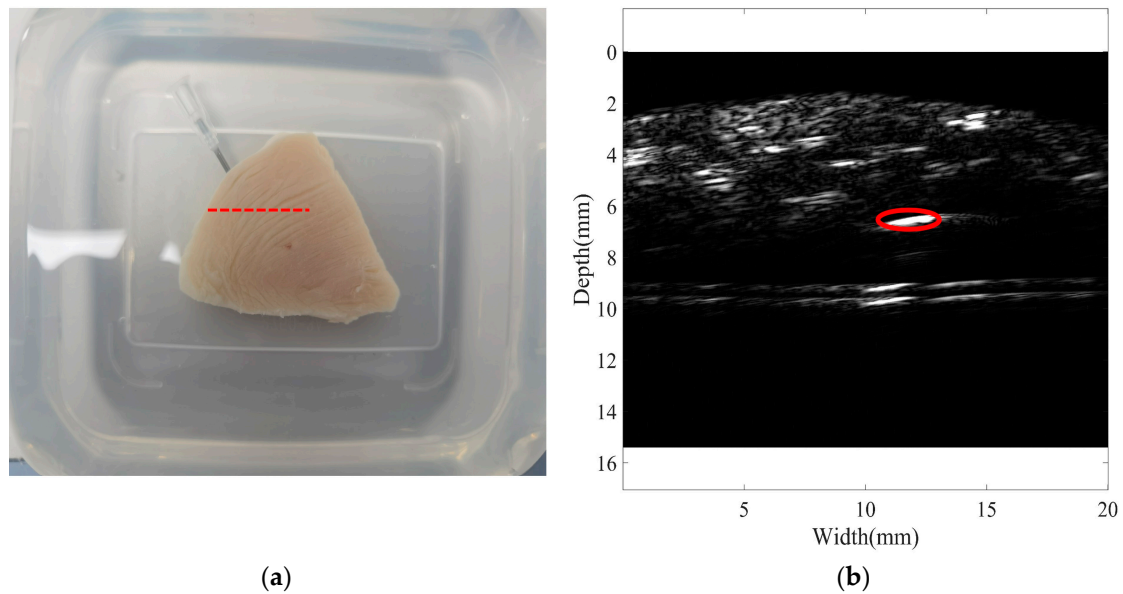


Figure 12. (a) Photograph of a biological sample with a needle inserted, with a red dashed line denoting the scan line. (b) Ex vivo ultrasound B-scan image of cross-section of the needle (highlighted with a red oval) inserted into the sample.

4. Conclusions

In this study, 2.5Sm-0.72PMN-0.28PT was synthesized for the development of 1-3 ceramic/epoxy composite material. With a ceramic volume fraction of 60%, the composite was successfully fabricated through the dice-and-fill method, showing a high piezoelectric constant and clamped dielectric constant. A miniature 12.4-MHz ultrasound transducer with an aperture size of $0.84 \text{ mm} \times 0.84 \text{ mm}$ was fabricated using the developed composite. In comparison to ultrasound transducers fabricated using alternative piezoelectric 1-3 composites, the aperture size could be reduced to only 1/7 while maintaining an optimized electrical matching design. The achieved -6 dB bandwidth and insertion loss were found to be satisfactory when compared to other transducers with similar structures. Tungsten wire imaging was conducted to evaluate the axial and lateral resolutions, and ex vivo imaging was conducted to prove the capability of the miniature transducer for biomedical imaging applications.

This study has some limitations. Firstly, the imaging quality was suboptimal, possibly attributed to the low frequency of the transducer. Additionally, the experimental waveforms of pulse-echo response and bandwidth exhibited slight discrepancies compared to the simulation results. One potential explanation could be the width-to-height aspect ratio approaching the threshold value, where transverse vibration modes may impact the transducer performance.

The future work involves advancing transducer technology by incorporating higher frequencies ($>30 \text{ MHz}$) through the utilization of Sm-PMN-PT composite materials, aiming to enhance imaging quality. However, achieving this goal requires the integration of picosecond laser cutting technology to produce narrower kerfs [40].

Concurrently, as ultrasound transducers with higher frequencies inherently demand smaller optimal apertures, there will arise a potential compromise in sensitivity. To address this challenge, exploring alternative methods such as alternating current polarization and conducting in-depth investigations into the composition and synthesis of piezoelectric ceramics could offer viable solutions to improve the overall transducer performance. Furthermore, the optimization of the matching layer is imperative, involving a thorough study of material characteristics and thickness [34]. This exploration has the potential to enable transducer operation away from transverse vibration mode, thereby maximizing ultrasound transmission efficiency.

Author Contributions: Conceptualization, K.-H.L. and J.-M.Z.; Methodology, J.-M.Z., W.G., R.-Q.L. and G.-C.B.; Data curation, J.-M.Z., G.-C.B., R.-Q.L. and F.Y.; Writing—original draft preparation, J.-M.Z. and G.-C.B.; Writing—review and editing, K.-H.L.; Supervision, Funding acquisition, K.-H.L. All authors have read and agreed to the published version of the manuscript.

Funding: The authors gratefully acknowledge support from the Hong Kong Research Impact Fund (R5029-19) and the Hong Kong General Research Fund (15220920).

Data Availability Statement: Data are contained within the article.

Conflicts of Interest: The authors declare no conflicts of interest.

References

- Chen, Y.; Lam, K.H.; Zhou, D.; Cheng, W.; Dai, J.; Luo, H.; Chan, H. High-frequency PIN-PMN-PT single crystal ultrasonic transducer for imaging applications. *Appl. Phys. A* **2012**, *108*, 987–991. [\[CrossRef\]](#)
- Wells, P.N.; Liang, H.-D. Medical ultrasound: Imaging of soft tissue strain and elasticity. *J. R. Soc. Interface* **2011**, *8*, 1521–1549. [\[CrossRef\]](#)
- Chan, V.; Perlas, A. Basics of ultrasound imaging. In *Atlas of Ultrasound-Guided Procedures in Interventional Pain Management*; Springer: New York, NY, USA, 2011; pp. 13–19.
- Haertling, G.H. Ferroelectric ceramics: History and technology. *J. Am. Ceram. Soc.* **1999**, *82*, 797–818. [\[CrossRef\]](#)
- Lu, X.M.; Proulx, T. Single Crystals vs. PZT Ceramics for Medical Ultrasound Applications. In Proceedings of the IEEE Ultrasonics Symposium, Rotterdam, The Netherlands, 18–21 September 2005; pp. 227–230.
- Edwards, G.; Chan, H.; Batten, A.; Lam, K.H.; Luo, H.; Scott, D. PMN-PT single-crystal transducer for non-destructive evaluation. *Sens. Actuator A Phys.* **2006**, *132*, 434–440. [\[CrossRef\]](#)
- Gururaja, T.; Schulze, W.A.; Cross, L.E.; Newnham, R.E.; Auld, B.A.; Wang, Y.J. Piezoelectric composite materials for ultrasonic transducer applications. Part I: Resonant modes of vibration of PZT rod-polymer composites. *IEEE Trans. Sonics Ultrason* **1985**, *32*, 481–498. [\[CrossRef\]](#)
- Newnham, R.E.; Skinner, D.P.; Cross, L.E. Connectivity and piezoelectric-pyroelectric composites. *Mater. Res. Bull.* **1978**, *13*, 525–536. [\[CrossRef\]](#)
- Smith, W.A.; Auld, B.A. Modeling 1-3 composite piezoelectrics: Thickness-mode oscillations. *IEEE Trans. Ultrason Ferroelectr. Freq. Control* **1991**, *38*, 40–47. [\[CrossRef\]](#)
- Ritter, T.; Geng, X.; Shung, K.K.; Lopath, P.D.; Park, S.-E.; Shrout, T.R. Single crystal PZN/PT-polymer composites for ultrasound transducer applications. *IEEE Trans. Ultrason Ferroelectr. Freq. Control* **2000**, *47*, 792–800. [\[CrossRef\]](#)
- Klicker, K.; Biggers, J.; Newnham, R. Composites of PZT and epoxy for hydrostatic transducer applications. *J. Am. Ceram. Soc.* **1981**, *64*, 5–9. [\[CrossRef\]](#)
- Chan, H.L.-W.; Li, K.; Choy, C.-L. Piezoelectric ceramic fibre/epoxy 1-3 composites for high-frequency ultrasonic transducer applications. *Mater. Sci. Eng. B* **2003**, *99*, 29–35. [\[CrossRef\]](#)
- Wang, D.Y.; Li, K.; Chan, H.L.W. High frequency 1-3 composite transducer fabricated using sol-gel derived lead-free BNBT fibers. *Sens. Actuator A Phys.* **2004**, *114*, 1–6. [\[CrossRef\]](#)
- Chen, Y.; Mei, K.; Wong, C.-M.; Lin, D.; Chan, H.L.W.; Dai, J. Ultrasonic Transducer Fabricated Using Lead-Free BFO-BTO+Mn Piezoelectric 1-3 Composite. *Actuators* **2015**, *4*, 127–134. [\[CrossRef\]](#)
- Zheng, T.; Zhang, Y.; Ke, Q.; Wu, H.; Heng, L.W.; Xiao, D.; Zhu, J.; Pennycook, S.J.; Yao, K.; Wu, J. High-performance potassium sodium niobate piezoceramics for ultrasonic transducer. *Nano Energy* **2020**, *70*, 104559. [\[CrossRef\]](#)
- Ke, Q.; Liew, W.H.; Tao, H.; Wu, J.; Yao, K. KNNS-BNZH lead-free 1–3 piezoelectric composite for ultrasonic and photoacoustic imaging. *IEEE Trans. Ultrason Ferroelectr. Freq. Control* **2019**, *66*, 1395–1401. [\[CrossRef\]](#)
- Yan, P.; Qin, Y.; Xu, Z.; Han, F.; Wang, Y.; Wen, Z.; Zhang, Y.; Zhang, S. Highly transparent Eu-doped 0.72 PMN-0.28 PT ceramics with excellent piezoelectricity. *Acs Appl. Mater. Inter.* **2021**, *13*, 54210–54216. [\[CrossRef\]](#)
- Li, C.; Xu, B.; Lin, D.; Zhang, S.; Bellaiche, L.; Shrout, T.R.; Li, F. Atomic-scale origin of ultrahigh piezoelectricity in samarium-doped PMN-PT ceramics. *Phys. Rev. B* **2020**, *101*, 140102. [\[CrossRef\]](#)
- Bao, G.-C.; Shi, D.-L.; Zhang, J.-M.; Yang, F.; Yang, G.; Li, K.; Fang, B.-J.; Lam, K.-H. Samarium-doped lead magnesium niobate-lead titanate ceramics fabricated by sintering the mixture of two different crystalline phases. *Materials* **2023**, *16*, 6781. [\[CrossRef\]](#)
- Savakus, H.; Klicker, K.; Newnham, R. PZT-epoxy piezoelectric transducers: A simplified fabrication procedure. *Mater. Res. Bull.* **1981**, *16*, 677–680. [\[CrossRef\]](#)
- Jiang, L.; Chen, R.; Xing, J.; Lu, G.; Li, R.; Jiang, Y.; Kirk Shung, K.; Zhu, J.; Zhou, Q. Fabrication of a (K,Na)NbO₃-based lead-free 1–3 piezocomposite for high-sensitivity ultrasonic transducers application. *J. Appl. Phys.* **2019**, *125*, 214501. [\[CrossRef\]](#)
- Wong, C.; Chan, S.; Liu, R.; Zhang, J.; Wu, W.; Liang, Z.; Yau, H.; Wang, D.; Li, S.; Lam, K. 20-MHz phased array ultrasound transducer for in vivo ultrasound imaging of small animals. *Ultrasonics* **2022**, *126*, 106821. [\[CrossRef\]](#)
- Cannata, J.M.; Ritter, T.A.; Chen, W.-H.; Silverman, R.H.; Shung, K.K. Design of efficient, broadband single-element (20–80 MHz) ultrasonic transducers for medical imaging applications. *IEEE Trans. Ultrason Ferroelectr. Freq. Control* **2003**, *50*, 1548–1557. [\[CrossRef\]](#)

24. Fan, D.; Niu, H.; Liu, K.; Sun, X.; Wang, H.; Shi, K.; Mo, W.; Jian, Z.; Wen, L.; Shen, M. Nb and Mn co-modified $\text{Na}_{0.5}\text{Bi}_{4.5}\text{Ti}_4\text{O}_{15}$ bismuth-layered ceramics for high-frequency transducer applications. *Micromachines* **2022**, *13*, 1246. [[CrossRef](#)]
25. Chiu, C.T.; Kang, B.J.; Eliahoo, P.; Abraham, T.; Shung, K.K. Fabrication and characterization of a 20-MHz microlinear phased-array transducer for intervention guidance. *IEEE Trans. Ultrason. Ferroelectr. Freq. Control* **2017**, *64*, 1261–1268. [[CrossRef](#)]
26. Guo, Q.; Hou, L.; Li, F.; Xia, F.; Wang, P.; Hao, H.; Sun, H.; Liu, H.; Zhang, S. Investigation of dielectric and piezoelectric properties in aliovalent Eu^{3+} -modified $\text{Pb}(\text{Mg}_{1/3}\text{Nb}_{2/3})\text{O}_3\text{-PbTiO}_3$ ceramics. *J. Am. Ceram. Soc.* **2019**, *102*, 7428–7435. [[CrossRef](#)]
27. Li, F.; Lin, D.; Chen, Z.; Cheng, Z.; Wang, J.; Li, C.; Xu, Z.; Huang, Q.; Liao, X.; Chen, L.-Q. Ultrahigh piezoelectricity in ferroelectric ceramics by design. *Nat. Mater.* **2018**, *17*, 349–354. [[CrossRef](#)] [[PubMed](#)]
28. Yang, Y.; Sun, E.; Xu, Z.; Zheng, H.; Yang, B.; Zhang, R.; Cao, W. Elimination of pyrochlore phase in high-concentration Sm^{3+} -doped PMN-PT piezoelectric ceramics by excessive MgO. *J. Am. Ceram. Soc.* **2022**, *105*, 4180–4190. [[CrossRef](#)]
29. M'Peko, J.-C.; Peixoto, A.G.; Jiménez, E.; Gaggero-Sager, L.M. Electrical properties of Nb-doped PZT 65/35 ceramics: Influence of Nb and excess PbO. *J. Electroceramics* **2005**, *15*, 167–176. [[CrossRef](#)]
30. Uchino, K.; Nomura, S. Critical exponents of the dielectric constants in diffused-phase-transition crystals. *Ferroelectrics* **1982**, *44*, 55–61. [[CrossRef](#)]
31. Fang, Z.; Tian, X.; Zheng, F.; Jiang, X.; Ye, W.; Qin, Y.; Wang, X.; Zhang, Y. Enhanced piezoelectric properties of Sm^{3+} -modified PMN-PT ceramics and their application in energy harvesting. *Ceram. Int.* **2022**, *48*, 7550–7556. [[CrossRef](#)]
32. Zhang, Q. Ultrasonic Transducers for Acoustic Vortex Tweezing Application. Ph.D. Thesis, Hong Kong Polytechnic University, Hong Kong, China, 2020.
33. Shen, Z.Y.; Li, J.F.; Chen, R.; Zhou, Q.; Shung, K.K. Microscale 1–3-type $(\text{Na,K})\text{NbO}_3$ -based Pb-free piezocomposites for high-frequency ultrasonic transducer applications. *J. Am. Ceram. Soc.* **2011**, *94*, 1346–1349. [[CrossRef](#)] [[PubMed](#)]
34. Li, Z.; Shao, W.; Zhu, X.; Lv, J.; Han, Z.; Cui, Y. Parylene coating for 13 MHz 1-3 composite transducer performance enhancement. *Appl. Acoust.* **2021**, *174*, 107696. [[CrossRef](#)]
35. Jiang, L.; Chen, H.; Zeng, Y.; Tan, Z.; Wu, J.; Xing, J.; Zhu, J. Potassium sodium niobate-based lead-free high-frequency ultrasonic transducers for multifunctional acoustic tweezers. *ACS Appl. Mater. Inter.* **2022**, *14*, 30979–30990. [[CrossRef](#)] [[PubMed](#)]
36. Jadidian, B.; Hagh, N.M.; Winder, A.A.; Safari, A. 25 MHz ultrasonic transducers with lead-free piezoceramic, 1–3 PZT fiber-epoxy composite, and PVDF polymer active elements. *IEEE Trans. Ultrason. Ferroelectr. Freq. Control* **2009**, *56*, 368–378. [[CrossRef](#)] [[PubMed](#)]
37. Sun, P.; Zhou, Q.; Zhu, B.; Wu, D.; Hu, C.; Cannata, J.M.; Tian, J.; Han, P.; Wang, G.; Shung, K.K. Design and fabrication of PIN-PMN-PT single-crystal high-frequency ultrasound transducers. *IEEE Trans. Ultrason. Ferroelectr. Freq. Control* **2009**, *56*, 2760–2763. [[PubMed](#)]
38. Zhang, Q.; Pang, X.; Zhang, Z.; Su, M.; Hong, J.; Zheng, H.; Qiu, W.; Lam, K.H. Miniature transducer using PNN-PZT-based ceramic for intravascular ultrasound. *IEEE Trans. Ultrason. Ferroelectr. Freq. Control* **2019**, *66*, 1102–1109. [[CrossRef](#)] [[PubMed](#)]
39. Liu, J.-B.; Miller, L.S.; Bagley, D.H.; Goldberg, B.B. Endoluminal sonography of the genitourinary and gastrointestinal tracts. *J. Ultrasound Med.* **2002**, *21*, 323–337. [[CrossRef](#)]
40. Lei, Z.; Xu, G.; Liu, J.; Liu, Y.; Ji, X. Micromachining of high-quality PMN-PT/epoxy 1-3 composite for high-frequency (>30 MHz) ultrasonic transducer applications. *IEEE Trans. Ultrason. Ferroelectr. Freq. Control* **2023**, *70*, 1563–1573. [[CrossRef](#)]

Disclaimer/Publisher's Note: The statements, opinions and data contained in all publications are solely those of the individual author(s) and contributor(s) and not of MDPI and/or the editor(s). MDPI and/or the editor(s) disclaim responsibility for any injury to people or property resulting from any ideas, methods, instructions or products referred to in the content.